Solved and Unsolved Problems in Ion-Beam Analysis: The Influence of Single Collisions

P.L. Grande[1,*], A. Hentz[1], R.P. Pezzi[1,2], I.J.R. Baumvol[1,3] and G. Schiwietz[4]

[1]Instituto de Física da Universidade Federal do Rio Grande do Sul
Avenida Bento Gonçalves 9500
91501-970, Porto Alegre, RS, Brazil
[2]IBM Research Division, T.J. Watson Research Center
P.O. Box 218, Yorktown Heights, NY 10598, USA
[3]Centro de Ciências Exatas e Tecnologia, UCS
Caxias do Sul, R.S., Brazil 95070-560
[4]Hahn-Meitner-Institut, Abteilung SF4
Glienicker Str. 100, 14109 Berlin, Germany

Abstract

In this work we explore some unsolved problems in ion-beam techniques involving backscattered projectiles or nuclear reactions. In particular, we focus on the influence of a single violent collision on the depth resolution. In high-resolution experiments, where the surface or near surface interfaces are investigated, the energy straggling becomes very asymmetric. The corresponding energy-loss distributions are skewed for larger energy losses due to the ionization and excitation of the inner-shell electrons. We determine the electronic energy-loss distribution using the coupled-channel calculations. Then these *ab-initio* calculations are used as benchmark for simple models of energy-loss lineshapes that can be used in ion-beam analysis to replace the standard Gaussian distribution.

* E-mail: grande@if.ufrgs.br

Contents

1. Introduction

The ideal ion-beam technique is the one that is non-destructive, has high sensitivity, atomic selectivity and high lateral and well as depth resolution.

However, this is not the case for the real ion-beam techniques. In fact, most of the open problems in ion-beam analysis (IBA) are concerned with how to increase sensitivity and resolution without damaging the target.

Many improvements have been achieved during the last years in order to increase sensitivity and resolution in IBA. From the experimental point of view, the increasing use of magnetic, electrostatic and time-of-flight spectrometers has strongly enhanced the resolution compared to standard surface barrier detectors. The detection efficiency has been improved by using a larger number of detectors

as well as by increasing the solid angle with the corresponding geometrical corrections (Dollinger et al., 2004). Furthermore, ultra high vacuum conditions have allowed for surface and near-surface investigations (Woodruff and Delchar, 1994). On the side of the data analysis, nowadays there are many fitting procedures and simulation programs, which have been recently reviewed by Rauhala et al. (2006). From the theoretical point of view, the equilibrium and non-equilibrium stopping forces as function of the projectile charge-state can be obtained using different approaches and programs, as for example the Unitary Convolution Approximation UCA (Schiwietz and Grande, 1999; Grande and Schiwietz, 2002), the Friedel Sum extended to finite velocities (Arista and Lifschitz, 1998; Arista, 2002) and the Binary model (Sigmund and Schinner, 2000, 2002; Sigmund, 2004). In these approaches the projectile charge-state enters as an input parameter. Recently, Grüner and Bell (2006) has extended the CTMC (Classical Trajectory Monte-Carlo) method (Olson, 1989) to calculate not only the stopping force but also the charge-states for heavy ions at high energies. Concerning the statistical treatment, the use of the stochastic theory to analyze, for instance, the nuclear reaction analysis (NRA) using nuclear resonant reactions, has established this ion-beam technique as a powerful method for depth profiling light isotopes (Maurel et al., 1982).

The improved experimental conditions have allowed for energy resolved monolayer resolution, using medium energy ion scattering (MEIS) (Vrijmoeth et al., 1991), Rutherford backscattering (RBS) (Kimura et al., 1994) and also recoil detection analysis (ERDA) (Dollinger et al., 1998b). The fundamentals for monolayer resolution analytics using the energy loss of ionic projectiles is, besides the high resolution, grazing incidence or detection conditions (only few degrees with respect to the surface), because the ratio of the energy loss straggling to the mean energy loss decreases for increasing projectile pathlength. Recently, Carstanjen and coworkers (Srivastava et al., 2004) have performed a remarkable experiment, where individual atom layers in graphite have been observed by RBS using 1 MeV N projectiles. In this experiment we may find two open problems in IBA, namely a non-Gaussian energy loss distribution for atomic layers near the surface and a reduced yield for the first monolayer due to charge exchange processes.

The present paper is organized as follows. Some unsolved problems in IBA are addressed in Section 2. Then, we will focus on the problem of asymmetric energy loss distributions in Section 3 and subsequent sections. The energy loss straggling in a single collision (in Section 4) will be described using *ab-initio* calculations (in Sections 4.1 to 4.4) and a simplified model (in Section 4.5). The importance and correct modeling of the energy loss in a single collision is discussed in Section 5 for depth profiling of Hf in sub-nanometric high-k oxide films (in Section 5.1)

and for the description of the surface peak in Al (in Section 5.2). Finally the conclusions are presented in the last section. If not indicated otherwise, atomic units ($e = m = \hbar = 1$) will be used throughout the paper.

2. Open Problems in IBA

In most used ion-beam techniques including analysis (RBS, MEIS, ERDA, NRA, etc.) (Tesmer and Nastasi, 1995) and ion therapy (Debus et al., 2004), the energy scale can be converted to depth and the measured yield to concentration. In this way, the accurate knowledge of the projectile energy-loss distribution and charge-states are of fundamental importance. Not only the knowledge of stopping forces are required but also the energy straggling (Gaussian or non-Gaussian) as a function of the projectile charge-state must be accurately known, even within a 1% level, for some applications.

For ion-beam techniques dealing with heavy ions, there are additional problems in the data analysis related to non-equilibrium projectile charge-states. It has been observed (Dollinger et al., 1998a; Carstanjen, 1998) that the yield of detected heavy ions depends on the projectile charge-state and the charge-state populations depend on the depth. In fact, the correct data analysis in such experiments is a quite complex problem, since many charge-changing cross-sections have to be known accurately as a function of the projectile charge and energy. An experimental way out of this problem is the measurement of the yield for all projectile-charge states, which is extremely time consuming especially for electrostatic and magnetic spectrometers.

There are numerous other problems, which limit the use of ion-beam analysis. For instance, it would be very interesting to use ion-beam techniques for elemental depth profiling in materials that are not planar such as nanostructures embedded in a homogenous host target. However, all data analysis procedures assume translation invariance in the direction perpendicular to the sample normal.

Another problem is the determination of the instrumental resolution function without any influence of the target, particularly in magnetic and electrostatic spectrometers (Munoz-Marquez et al., 2005b). In fact, what can be measured is the convolution of the instrumental spectrometer function with the energy-loss straggling. The accurate knowledge of the instrumental function as well as of the Doppler effect coming from target thermal vibrations are of ultimate importance to understand the asymmetric energy-loss distributions in future ultra-high resolution experiments.

Among many open problems for ion-beam analysis, here we will focus our present study to address asymmetric energy-loss distribution laws. As will be

shown below, the understanding and corresponding modeling of such asymmetries is crucial to use the ion-beam analysis in subnanometric regions near the surface.

3. Asymmetric Energy Loss Straggling

The use of Gaussian distributions for the electronic energy loss in IBA techniques has been widely used in the literature not only because its simplicity but also because for thick enough targets the energy-loss distribution does tend to a normal distribution according to the central limit theorem (for $\Omega^2 \gg T_{\max}^2$ – see Sigmund, 2006). In other words, a Gaussian energy-distribution results from the convolution of many small energy losses due to individual events.

There are two significant improvements of the existing formalism: impact-parameter-dependent straggling (Kabachnik et al., 1993) (adopted here) and non-Gaussian straggling based on realistic and non-realistic energy-transfer cross-sections (for a very nice and self containing review, see Sigmund, 2006).

Differently from other ion-beam techniques, the modeling of nuclear reaction profiling (NRP) (Maurel et al., 1982) does not assume Gaussian energy-loss distributions. Instead many self-convolutions are determined numerically for an approximate single collision spectrum. The nuclear reaction yield is then obtained by considering Poisson statistics of collisions, the cross-section for the resonant reaction, the beam spread and Doppler broadening effect. Thus, experimental excitation curves are fitted using trial concentration profiles. In this way, highly accurate depth profiling of light isotopes has been obtained with remarkable depth resolution (Driemeier et al., 2006), though the electronic excitations for the ion-nucleus nuclear reaction are also important for an improved depth resolution in ultra-thin films (Schulte et al., 2001).

In summary, the asymmetry in the energy-loss distribution arises from the statistics of collisions, which are uncorrelated in amorphous materials and correlated in crystals. On the other hand, collisions with very small impact parameters to the nucleus as the backscattering collision in scattering techniques may be responsible for very large asymmetries since the inner-shells can be ionized. This will be of ultimate importance for the cases where there are collisions with high inner-shell ionization probability and large binding energy.

Moreover, the inner-shell binding energy has to exceed the projectile-energy straggling before the violent collision, and of course, the experimental resolution must have a variance smaller than (or comparable to) the inner-shell binding energy. This scenario occurs, for instance, in surface and near-surface investigations using typically few hundred keV of protons or helium in MEIS experiments (Hoshino et al., 2005).

4. Energy Loss in a Single Collision

During the last years we have investigated the electronic energy loss of bare and screened ions for light targets using the coupled-channel method. This first principle calculation (Schiwietz, 1990; Grande and Schiwietz, 2004), based on an expansion of the time-dependent electronic wave function in terms of atomic orbitals, has been successfully applied to evaluate the impact-parameter and angular dependence of the electronic energy loss and the total stopping cross-section of ions (antiprotons, H and He) colliding with H and He atoms at energies ranging between 1 to 500 keV/amu. It has also been applied to calculate the entrance-angle dependence of the stopping force for He ions channeling along the Si main crystal directions (dos Santos et al., 1997) as well the shape of the surface peak for protons backscattered from Al under channeling and blocking conditions (Grande et al., 2004).

These benchmark calculations have also been used to check simplified models that account for the basic energy loss processes without the need of large scale calculations (Grande and Schiwietz, 1998; Schiwietz and Grande, 1999) and to calculate the probability of multiphoton ionization in the case of intense fs-laser pulses (Schiwietz et al., 2001; Grande and Schiwietz, 2004).

4.1. Coupled-Channel Method

Here we will focus the attention on atomic treatments of the energy-transfer process. Thus, we will not consider solid-state effects such as intra-band transitions, collective excitations (bulk and surface plasmons) and the corresponding dynamic projectile screening. The coupled-channel was already reviewed in Grande and Schiwietz (2004). In what follows we review the most important points for completeness. Any additional information can be found in Grande and Schiwietz (2004) and references therein.

The theoretical formulation of atomic excitation and ionization processes is conveniently discussed by introducing the quantum-mechanical Hamilton operator. For a three-body system the Hamiltonian reads

$$\mathcal{H} = T_{\mathrm{p}}(\vec{r}_{\mathrm{p}}) + T_{\mathrm{t}}(\vec{r}_{\mathrm{t}}) + T_{\mathrm{e}}(\vec{r}_{\mathrm{e}}) + V_{\mathrm{pt}}(\vec{R}) + V_{\mathrm{te}}(\vec{r}) + V_{\mathrm{pe}}(\vec{R} - \vec{r}) \tag{1}$$

with the kinetic and potential energies denoted T and V, respectively. The subscripts p, t, and e refer to the projectile ion, target core, and electron as indicated in Figure 1.

In the following we will use the impact-parameter method, i.e., it is assumed that $\vec{r}_{\mathrm{p}}$ and $\vec{r}_{\mathrm{t}}$ are given by classical paths $\vec{r}_{\mathrm{p}} = \vec{r}_{\mathrm{p}}(t, b)$, $\vec{r}_{\mathrm{t}} = \vec{r}_{\mathrm{t}}(t, b)$ (determined

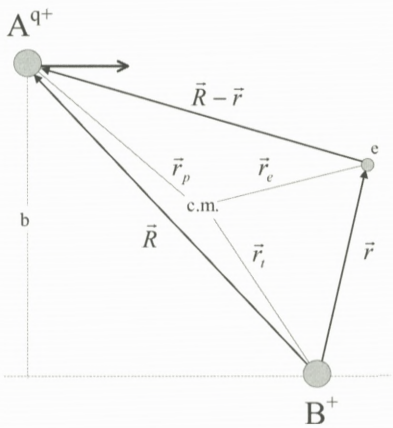

Figure 1. Vector diagram for the projectile ion A^{q+}, the ionic target core B^+, and one active electron. The impact parameter b is indicated. $\vec{r}_p$, $\vec{r}_t$ and $\vec{r}_e$ are position vectors of projectile, target, and electron in the center-of-mass system.

by the impact parameter b). This concept was first introduced by Mott (1931) and Bang and Hansteen (1959).

If, additionally, an independent motion of the electron (McGuire and Weaver, 1977) is assumed, one may solve the time-dependent Schrödinger equation for one active electron:

$$\left(i\frac{\partial}{\partial t} - \mathcal{H}_e\right)\Phi_e(t) = 0 \tag{2}$$

with

$$\mathcal{H}_e(t) = \mathcal{H}_{te} + V_{pe}(\vec{R}(t) - \vec{r}) \tag{3}$$

and

$$\mathcal{H}_{te}(t) = T_e(\vec{r}_e) + V_{te}(\vec{r}_e - \vec{r}_t(t)). \tag{4}$$

In the subsequent treatment the electron coordinate will be measured from the accelerated target nucleus and is the only dynamical variable. Thus the target system is the frame of reference. In such a non-inertial system non-Newtonian forces arise. The corresponding Hamiltonian $\mathcal{H}_{te}$ is

$$\mathcal{H}_{te} = -V_{te}(\vec{r}) + T_e(\vec{r}) + V_{recoil}(\vec{r}, \vec{r}_t(t)). \tag{5}$$

It is reasonable to neglect the last term V_{recoil}. By doing this, transitions are excluded which are due to the interaction of the active electron with the recoiling

target nucleus. This so-called recoil effect leads to insignificant contributions to total cross-sections, but may be important for very close collisions ($b < 10^{-3}$ a.u.) (Rösel et al., 1982). Before the solution of Equation (2) is explained in more detail, the classical path $\vec{R}(t)$ should be defined. Given the time-dependent electronic wave function Φ_e, a classical Hamiltonian for the heavy particles may be defined:

$$\mathcal{H}_h = T_p(\vec{r}_p) + T_t(\vec{r}_t) + V_{pt}(\vec{R}) + \langle \Phi_e | V_{pe}(\vec{R} - \vec{r}) | \Phi_e \rangle + \langle \Phi_e | V_{te}(\vec{r}) | \Phi_e \rangle. \quad (6)$$

With this Hamiltonian the classical equations of motion are solved. The last term in Equation (6) was neglected because of its small influence on the motion of the target core in case of a strongly target-centered wave function Φ_e. It is emphasized that the concept defined by Equation (6) introduces for the first time a dynamically curved projectile trajectory in the impact-parameter method. Thus the projectile motion is coupled to the motion of the active electron. We note that this procedure goes far beyond the Born–Oppenheimer approximation.

It is noted that some calculations have been performed with hyperbolic projectile paths. In this case only the first three terms in Equation (6) are considered. However, most of the previous calculations have been performed for straight line paths, as given by the first two terms in Equation (6). Such calculations are equivalent to quantum-mechanical solutions of the three-body Schrödinger equation with plane projectile waves.

4.2. Independent-Particle Model

The electronic many-body Hamiltonian in Equation (1) is treated in the framework of the independent-electron frozen-core model. This means that there is only one active electron, whereas the other electrons are passive (no dynamic correlation is accounted for) and no relaxation occurs. In this model the electron-electron interaction is replaced by an initial-state Hartree–Fock–Slater potential (Herman and Skillmann, 1963).

The independent-electron approximation allows for a distinction of target electrons and projectile-centered electrons which screen the projectile nuclear charge. One of the most important dynamic correlation effects (deviations from the independent-electron approximation) is the collision of a target electron with a projectile-centered electron (McGuire and Simony, 1981). This will directly enhance the energy loss and reduce the projectile screening.

The time-dependent Schrödinger equation may be solved by expanding $\Phi_e(\{\vec{r}\}, t)$ in terms of unperturbed eigenfunctions φ_i of the target with coefficients

$a_i(t) = \langle \varphi_i \mid \Phi_e(t) \rangle$. Thus, Equation (2) is replaced by a set of coupled first-order differential equations, the so-called coupled-channel equations:

$$i \frac{\mathrm{d}}{\mathrm{d}t} a_i(t) = \sum_j a_j(t)\, \mathrm{e}^{i(E_i - E_j)t} V_{j \to i}(\vec{R}(t)) \tag{7}$$

with the internuclear distance $\vec{R}$ and

$$V_{j \to i}(\vec{R}(t)) = \langle \varphi_i | V_{\mathrm{pe}}(\vec{R}(t), \vec{r}) | \varphi_j \rangle. \tag{8}$$

E_i is the orbital energy associated with the target wave function φ_i. Here V_{pe} is an effective potential seen by the active electron, which contains the screening effect produced by other electrons from the medium. For bare incident ions, the active-electron projectile interaction V_{pe} is just the Coulomb potential. However, in the case where the projectile carries electrons, we use a screened potential made up of the Coulomb part due to the projectile-nuclear charge and the static potential produced by the target electrons that screen the projectile-nuclear charge,

$$V_{\mathrm{pe}}(\vec{R} - \vec{r}) = -\frac{Z_{\mathrm{p}}}{|\vec{R} - \vec{r}|} + \sum_n^{\mathcal{N}} \int \mathrm{d}^3 r' \frac{|\chi_n(\vec{r'})|^2}{|\vec{R} - \vec{r} - \vec{r'}|}, \tag{9}$$

where Z_{p} is the projectile nuclear charge, χ_n is the projectile-electron wave function and $\mathcal{N}$ is the number of projectile electrons. The wave functions χ_n for each electron n of the projectile are obtained according to the Hartree–Fock–Slater procedure (Herman and Skillmann, 1963). Thus, we neglect dynamic screening (a time dependence of χ_n due to target induced polarization respectively excitation/ionization), Pauli correlation (antisymmetrization of the projectile- and target-centered wave functions) as well as dynamic correlation effects due to the residual electron-electron interaction. It is pointed out, that the dynamic electron-electron interaction is not included in the present model since there is only one active electron.

For high projectile speeds and low projectile charge-states the transition matrix-elements $V_{j \to i}$ are small. This is the domain of first-order perturbation theory (semi-classical approximation SCA, first-order Born approximation); see for example Kabachnik et al. (1993). In this case, most transitions are governed by the direct step from the initial state j to the final i. Thus, we may drop the summation over j and use $a_j(t) = 1$ (the state j corresponds to the ground-state). Hence, the time-consuming solution of the coupled-channel equations is reduced to a set of simple integrals over time within perturbation theory.

The coupled-channel equations are solved numerically in order to obtain the coefficients a_i after the collision ($t \to \infty$). In contrast to other coupled-channel

calculations we do not use pseudo states to represent the electron continuum wave functions. Instead we use a large number of continuum wave-packets that are composed out of a superposition of exact continuum eigenstates (up to 500 gerade states with partial waves up to $l = 10$), since the computation of the stopping power demands high accuracy of the emitted electron energy spectrum.

Each excited or continuum state corresponds to a well-defined energy transfer ΔE_i $(= E_i - E_0)$. Then the cross-section for a such an energy-transfer process will read

$$\sigma_i = 2\pi \int_0^\infty b \, \mathrm{d}b |a_i|^2(b) \tag{10}$$

and average electronic energy loss $Q(b)$ is given by

$$Q(b) = \sum_i |a_i|^2(b) \Delta E_i. \tag{11}$$

The electronic stopping cross-section S_e and energy straggling W per atom can be computed directly from:

$$S_\mathrm{e} = \sum_i \sigma_i \Delta E_i = 2\pi \int_0^\infty b \, \mathrm{d}b \; Q(b) \tag{12}$$

and

$$W = \sum_i \sigma_i \Delta E_i^2. \tag{13}$$

For the electronic energy-loss distribution $\mathrm{d}P_i/\mathrm{d}T$ we use

$$\frac{\mathrm{d}P_i}{\mathrm{d}T}(b) = \sum_f |a_{i\to f}(b)|^2 \delta(T - (\epsilon_f - \epsilon_i)), \tag{14}$$

It is pointed out that for elastic collisions $(f = i)$ as well as for "bound-state" excitation the energy-loss distribution defined above contains spikes due to the atomic level structure. Broadening effects originating from state lifetime, band width and the Doppler effect are not considered explicitly since they are much smaller than the experimental resolution. It is noted that the above sums have to be replaced by integrals in the case of continuum states.

4.3. Higher-Order Effects

The coupled-channel calculations allow for accurate calculations of higher-order effects. At high energies the electronic energy loss may be expanded in terms of the projectile charge Z_p according to

$$Q(b) = q_1 Z_p^2 + q_2 Z_p^3 + q_3 Z_p^4 + \cdots . \tag{15}$$

The quadratic term is the leading one at high energies. It is well described by first-order Born theory and involves only direct ionization and excitation of the target atom. With decreasing ion energy higher-order effects become important. They either depend on the sign of the projectile charge Z_p (polarization and binding effects) or only on the absolute value of Z_p. All higher-order effects (deviations from the Z_p^2 proportionality) can be related to multiple successive interactions of the active electron with the projectile and the (screened) target within a single collision. The number of these interactions increases for high projectile charges, small impact parameters and low projectile velocities. We can distinguish different higher-order contributions as a function of the strength of the perturbation.

For small perturbations of outer-shell electrons the polarization of the electronic density appears first. Positively charged particles attract and negatively charged projectiles repel the electron cloud during an early stage of the collision, which leads to a change of the density around the projectile path and correspondingly to a change in the stopping power. This is a second-order effect (proportional to Z_p^3).

By decreasing the ion energy the influence of the projectile is no longer a small perturbation and effects such as saturation and binding-energy modifications will appear. In standard first-order treatments, the sum over all probabilities exceeds one since no reduction of the of the initial-state population is accounted for. This leads to an artificial creation of electrons (overestimated stopping power proportional to Z_p^4). The corresponding experimentally observed saturation (stopping power reduction compared to Z_p^2 for heavy ions) may roughly be described within the unitary first-order Magnus approximation (Ryufuku and Watanabe, 1978, 1979). A different treatment by Bloch (1933) also takes into account this effect and the term proportional to Z_p^4 agrees quite well with the one from coupled-channel calculations.

For inner-shell electrons the so-called binding effect gains importance. The resulting change of the stopping power is proportional to Z_p^3 but its sign is opposite to the change induced by the polarization effect. The binding effect can be viewed as an increased binding energy of the bound electron in the vicinity of positively charged projectiles, which reduces the stopping power for small impact parameters (or large scattering angles).

Finally, at low energies the projectile represents a strong perturbation and effects such as electron capture for positive projectiles and adiabatic ionization (Fermi–Teller effect; Schiwietz et al., 1996) for negative charged projectiles turn out to be very important. The electron capture may be viewed as a very strong

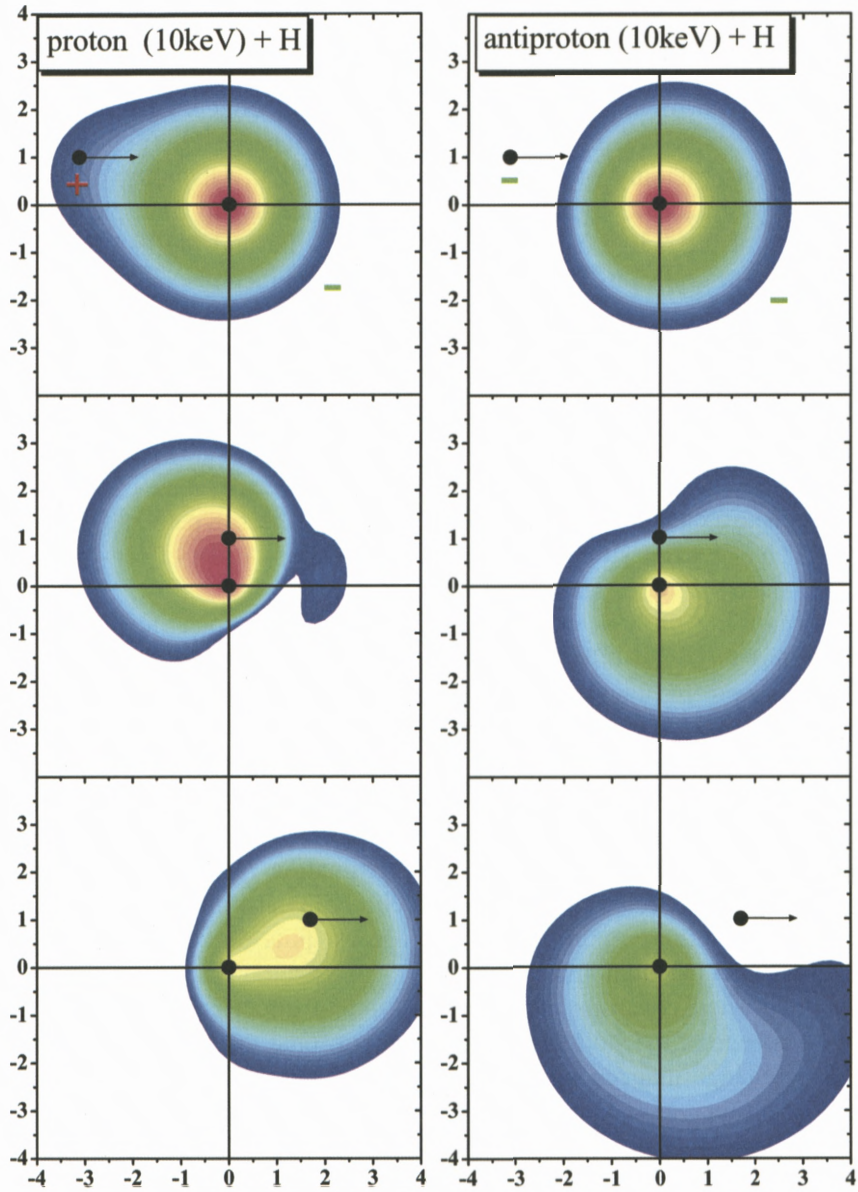

Figure 2. Contour plot of the time-dependent electronic density of a hydrogen atom disturbed by a 10keV proton (on the left) and antiproton (on the right) at $b = 1$. The plot corresponds to a cut of the density across the collision plane.

polarization effect (target electrons are attracted by and finally travel with the projectile). If the electronic motion is described in a target-centered basis all orders of the perturbation are necessary to yield the time-dependent electron-density. In other words, the interaction between electron and projectile never stops. In the Fermi–Teller effect, collisions with negative heavy projectiles are involved. For the case antiprotons on H, the electrons move in the field of a transient "quasidipole" formed by the heavy particles. The electronic states of the quasidipole experience a rapid loss of binding energy when the distance between the heavy particles decreases, and become even unbound at a certain non-zero "critical" distance.

Besides these effects we also observe for increasing perturbations (high Z_p at low energies) a diffusion-like effect in the energy spectrum of emitted electrons (Grande and Schiwietz, 1995). The first excitation step gives rise to an excitation spectrum with a maximum at low energy transfers. Successive interactions (continuum-continuum couplings) yield a broadening of the excitation spectrum. Hence, low electron energies are suppressed due to this diffusion-like process and the mean stopping power as well as the straggling are enhanced. This energy-diffusion effect may be viewed as the onset of the Fermi shuttle effect, where multiple head-on collisions between projectile and electron in the field of target lead to extremely high electron energies.

Figure 2 shows a contour plot of the time-dependent electron density for a hydrogen atom disturbed by a positively (displayed on left) and negatively (displayed on right) charged Coulombic point particle at 10 keV per atomic mass unit (amu) at an impact parameter of 1 a.u. These electronic densities correspond to a cut in the collision plane and were obtained directly from the calculated transition amplitudes $a_i(t)$ according to

$$\rho(\vec{r},t) = \sum_{i,j} a_i a_j^* \, \mathrm{e}^{-i(E_i-E_j)t} \varphi_i(\vec{r}) \varphi_j^*(\vec{r}), \tag{16}$$

using about 200 gerade states. An inspection of this figure shows several interesting features. First, the positively charged particle (proton) attracts the electron on the incoming path; the so-called polarization process. One may see that the electron density moves towards the projectile. The opposite effect takes place for the negatively charged particle (antiproton).

Second, for protons at the distance of closest approach, the maximum of the electron-density points to the backward direction at an angle of about 120 degrees with respect to the beam axis. It is clearly visible that the electron density lies behind the projectile, although the proton is attracting the electron. The reason for this behavior is a delayed response of the electron cloud (the inertia due to

the electron mass). Third, the proton enables electron-capture in the outgoing path of the collision and large fraction of the electron density is finally bound to and moving with the projectile. Since an antiproton repels the target-electron, the electron density near the projectile on the outgoing path of the collision is almost zero.

For collisions of antiprotons with atomic hydrogen, a quasi dipole is formed during the collisions. The dipolar antiproton-proton system does not support bound states for inter-particle distances below 0.64 a.u. (Schiwietz et al., 1996). For finite velocities and larger impact parameters b (in the figure, $b = 1$) there is still a significant ionization contribution. As can be observed in the figure at the distance of closest approach there is a high transition probability (blowing up of the density).

4.4. Reference Results

In the framework of the independent-electron model, the probability for a certain total electronic energy-loss ΔE transferred during an individual ion-atom collision can be written as

$$\frac{\mathrm{d}P_{\mathrm{atom}}^{\mathrm{elec}}}{\mathrm{d}\Delta E}(b) = \left(\prod_i \int \mathrm{d}T_i \, \frac{\mathrm{d}P_i}{\mathrm{d}T_i}(b)\right) \times \delta\left(\Delta E - \sum_i T_i\right), \tag{17}$$

where the index i runs over all electrons for each subshell, for example, the 1s, 2s, 2p, 3s and 3p of the Al atom. Equation (17) corresponds to a series of convolutions of individual single-electron energy-loss distributions from Equation (14). In this way, multiple ionizations/excitations are taken into account.

Figure 3 shows the results of the coupled-channel calculations for the energy-loss probability of 100 keV H^+ projectiles colliding with atomic Al at $b = 0$. The elastic peak (the peak at $\Delta E = 0$) is represented here by a Gaussian distribution with a very small standard deviation (about 10 eV) in order to keep the normalization and to avoid the use of a Dirac function. In the present case, backscattering is almost always accompanied by excitation or ionization events, involving mainly electrons from the 2p shell (due to the large number of electrons) and from the 3s and 3p bands. This is the reason for high backscattering yields at non-zero energies in the figure.

The main feature of the energy-loss distribution in Figure 3 is the significant contribution of the L-shell at large energy transfers. The contribution of the valence electrons for the surface peak is of minor importance since the corresponding M-shell energy loss is much smaller than the experimental resolution. K-shell ionization of Al atoms is kinematically suppressed for protons at incident energies below about 1 MeV.

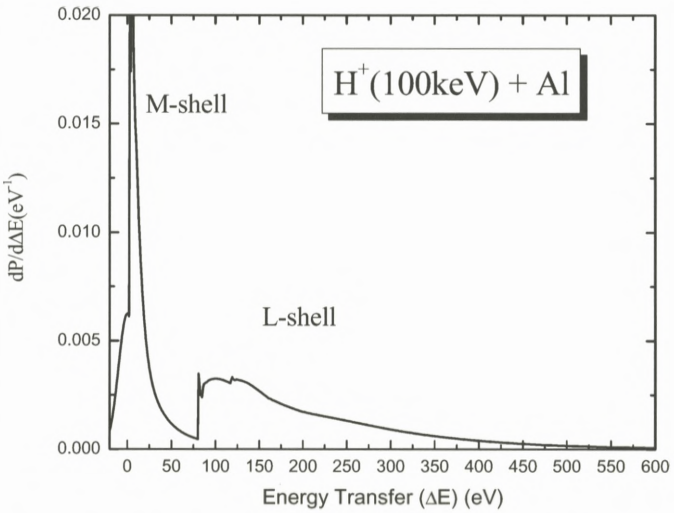

Figure 3. Energy transfer in a single collision for 100 keV H^+ on atomic Al for a near central collision ($b \rightarrow 0$).

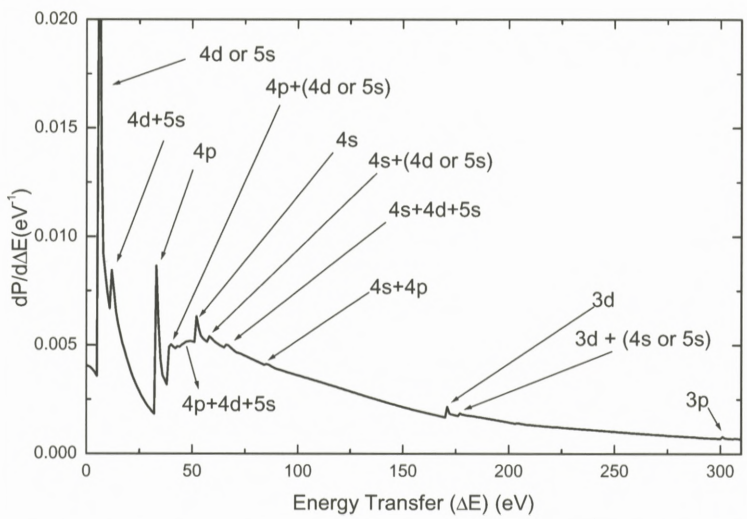

Figure 4. Energy transfer in a single collision for 100 keV H^+ on atomic Y for a near central collision ($b \rightarrow 0$).

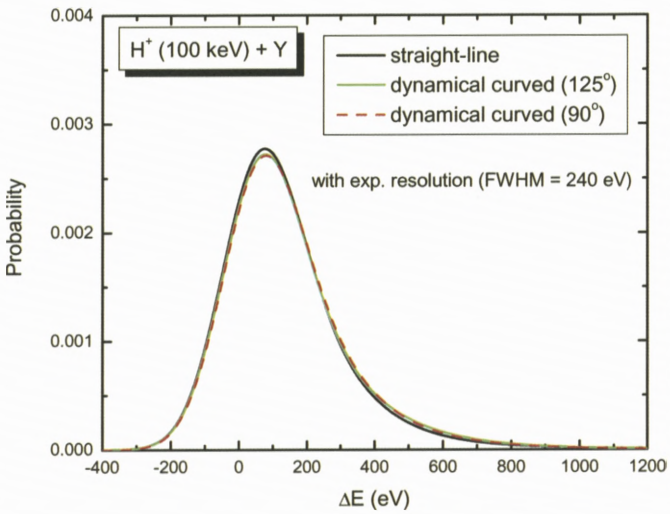

Figure 5. Energy transfer in a single collision for 100 keV H^+ on atomic Y using different projectile trajectories in a near central collision ($b \to 0$).

The same can be seen in Figure 4 but for an Y atom, which has much more subshells than Al. In this case we can observe many peaks indicated by arrows. Some of arising from double inner-shell ionization and even triple ionization are visible. However, all theses peaks are washed out after considering the experimental resolution or Doppler effect due to the thermal motion of the target atoms in a solid. But the energy-loss distribution remains very asymmetric (see Figure 5) because of large energy transfer to ionization of the inner-shells.

The influence of different ion trajectories on the electronic excitations can be seen in Figure 5 for 100 keV protons on Y atom. Here the coupled-channel results from Equation (17) were convoluted with a typical experimental resolution (of about 240 eV) found in MEIS experiments. The curve denoted as straight-line, corresponds to coupled-channel calculations using a straight-line trajectory for the projectile (passing through the Y atom) while the other curves stand for dynamic curved trajectories calculated from the hamiltonian described by Equation (6). For dynamic curved trajectories, the final scattering angle is indicated in Figure 5. As can be observed from this figure, the electronic energy-loss distribution is nearly insensitive to projectile trajectories as far as very small impact parameters are concerned. In fact there is a narrow range of impact parameters corresponding to a large variation of the scattering angle, where the energy-loss distribution is about the same (even for scattering angle of few degrees almost no change has

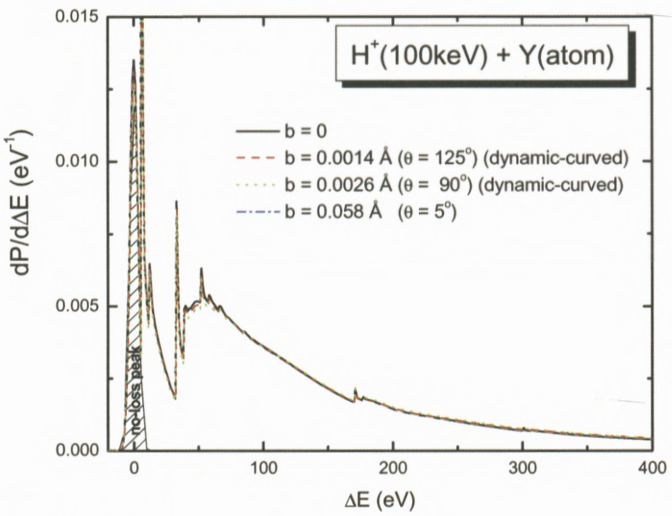

Figure 6. The same as in Figure 5 but unfolded results and including an additional scattering angle of 5 degrees.

been observed, see Figure 6). The *near central collision* regime is determined by this range of impact parameters. We have also checked the recoil effect described in Section 4.1 but it is negligible for protons with some hundred keV colliding with heavy targets such as Al or Y.

4.5. Simple Model for Energy-Loss Distributions

The coupled-channel calculations demand a computational effort that precludes its direct use in any analysis of ion-beam data. Therefore, we search for an approximate solution without the necessity of performing a large-scale calculation. For this purpose, the close coupling calculations shall be used as benchmark results to check simple models for the energy loss distribution at near central collisions. A detailed description of such models may be found elsewhere (Grande et al., 2006). Here we present only a short outline of the method.

4.5.1. *Model for the Mean Energy-Loss*

The first ingredient of a model for the electronic energy-loss distribution is the mean energy-loss value as a function of the impact parameter $Q(b)$. In recent works (Grande and Schiwietz, 1998; Schiwietz and Grande, 1999) we have proposed a simple formula for $Q(b)$ – called Perturbative Convolution Approximation (PCA) and Unitary Convolution Approximation (UCA) – realized by the CasP Program (Grande and Schiwietz, 2006). This formula reproduces first-order

Born results for all impact parameters for bare and also for screened projectiles (in the PCA mode) and contains some higher-order terms, reproducing the Bloch formula (Bloch, 1933) at high velocities (in the UCA mode). The UCA model can also be seen as the impact-parameter realization of the Bloch formula and resembles the Binary model of Sigmund and Schinner (2000). The following simple formula

$$Q(b) = \int \mathrm{d}^2 r_T \, \mathcal{K}(\vec{b} - \vec{r}_T) \int \mathrm{d}z \, \rho(\vec{r}_T, z) \tag{18}$$

with

$$\mathcal{K}(b) = \frac{2Z^2}{v^2 b^2} \times h\left(\frac{2vb}{\eta}\right) \times \sum_i f_i \, g\left(\frac{\omega_i b}{v}\right) \tag{19}$$

joins smoothly all regions of impact parameters b for which two-body ion-electron (small b) and dipole (large b) approximations are valid (see Figure 7).

The function $h(2vb)$ (see Grande and Schiwietz, 1998) approaches zero for $b \ll 1/v$ (relative impact parameter smaller than the electron de Broglie wavelength in the projectile frame) and it reaches 1 for large values of b. The first two product terms in Equation (19) resemble the classical energy transfer to a statistical distribution of electrons at rest and describe violent binary collisions. The last term, involving the g function (see Grande and Schiwietz, 1998) and the oscillator strengths f_i, accounts for the long ranged dipole transitions as depicted in fig(7) where the energy transfer is about $1/\Delta t$ (Δt is the collision time and is about the impact parameter b divided by the projectile velocity v). For intermediate impact-parameters the closure approximation in applicable (Grande and Schiwietz, 1998), which links smoothly the two body projectile-electron scenario with the dipole approximation.

The first integral $\int \mathrm{d}^2 r_T \ldots$, in Equation (18) describes a convolution with the initial electron density also outside the projectile path and yields non-local contributions to the energy loss. It is noted that these non-local contributions are neglected in most previous simple energy loss models. With the parameter η equal to one, this formula mimics the first-order Born approximation very well (Grande and Schiwietz, 1998) and it is denoted *PCA* (perturbative convolution approximation). For increasing projectile-charge first-order calculations (on which PCA is based) break down. They do not take in account, for instance, that each electron transition gives rise to an increased final-state population and a corresponding reduction of the initial state population. It is clear that the ionization probability cannot increase indefinitely with the strength of the perturbation (the so-called saturation effect). Since these ionization processes come mostly from

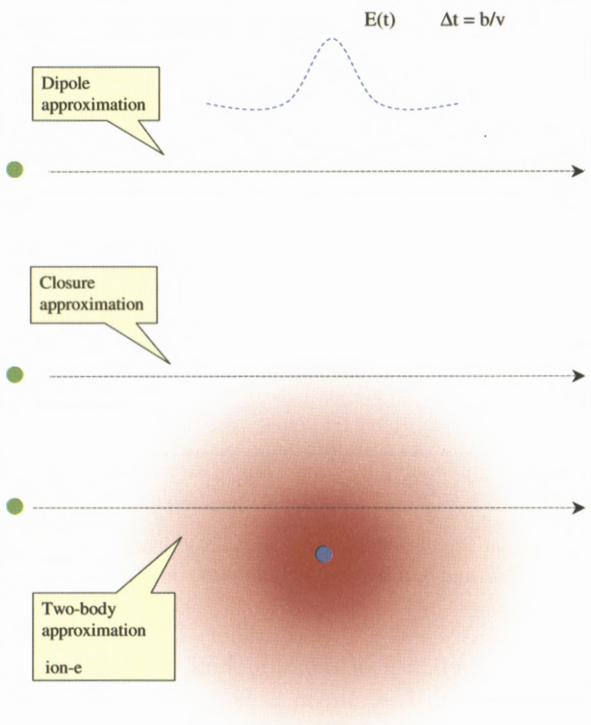

Figure 7. Impact parameter regions that are interpolated by the PCA/UCA models.

small impact parameters, we have introduced in Schiwietz and Grande (1999), a scaling parameter η in the function h that enforces unitarity in accordance with the Bloch model (Bloch, 1933).

Nevertheless, the UCA model, as other stopping power models (Sigmund and Schinner, 2002; Arista, 2002), only calculates the mean electronic energy loss. Except for the model from Grande et al. (2006) no simple calculation for the energy loss distribution as a function of the impact parameter is available so far.

4.5.2. *Energy-Loss Moments*

Using the mean energy loss $Q(b)$ calculated from the UCA model, as shown in Grande et al. (2006), we can determine the moments of the energy loss distribution by assuming the following model.

The energy-loss distribution due to a single electron in a given sub-shell has two parts. A no-loss part, represented by a delta function at zero energy transfer, and a loss part, separated from the no-loss part by an energy gap corresponding

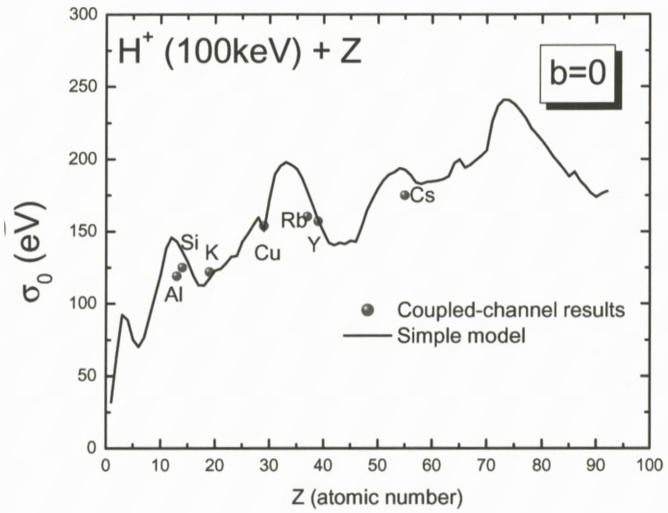

Figure 8. Standard deviation for the electronic energy-loss distribution in a single collision for impinging protons at 100 keV and $b = 0$ as a function of the atomic number of the target.

essentially to the binding energy of the sub-shell. The loss part involves a fixed averaged energy loss $\bar{E}$ (with $\bar{E} = \ln(2mv^2/I_b)$, where m is the electron mass, v the projectile velocity and I_b is the binding energy). The ratio of the loss to no-loss part (P_{reaction}), as a function of the impact parameters is determined from the mean energy loss $Q(b)$. The second and the third moments of the distribution, related to the standard deviation and skewness respectively, are determined by assuming a $1/\Delta E^2$ law starting from the binding energy value I_b up to the maximum energy transfer $2mv^2$. Then, the effect of all electrons is determined by adding the moments (relative to the first moment) according to the additivity rule found in convolutions of probability distributions. Further details can be found in Grande et al. (2006).

Figure 8 displays the results of this simple model for the standard deviation of the electronic energy-loss spectrum as a function of the atomic number of the target, for impinging 100 keV protons at an impact parameter close to zero (near central collision). The results are compared to coupled-channel results (Grande et al., 2006). In general the agreement is very good although some significant deviations can be observed. We note that the maxima and minima are not related the valence structure. Indeed they are due to the interplay between inner-shell ionization probability and binding energy.

Nonetheless, despite of the crudeness of the present model, it may be already sufficiently accurate to be used in MEIS or other ion-beam technique.

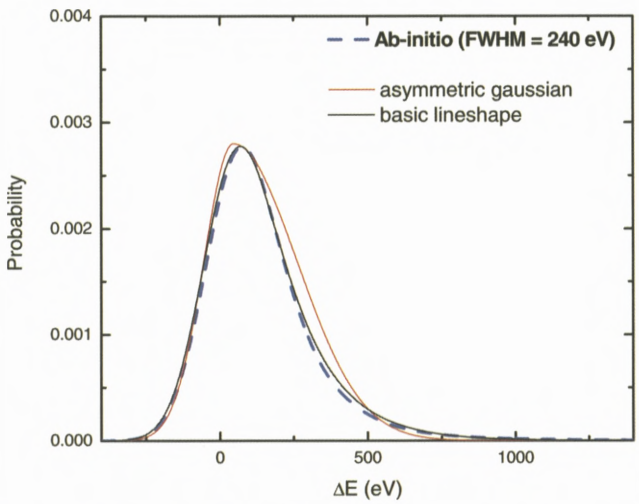

Figure 9. Coupled-channel results for 100 keV proton colliding with Y at a impact-parameter close to zero in comparison with analytical formulas. All results have been convoluted with the experimental resolution of 240 eV.

4.5.3. *Analytical Formula*

The coupled-channel calculations have also been used (see Grande et al., 2006) as a benchmark for simple analytical formulas of the electronic energy-loss distribution, which replace the Gaussian distribution when the asymmetry cannot be neglected.

In Figure 9 two analytical formulas for the energy-loss distribution are compared with coupled-channel results for 100 keV protons colliding with a Y atom at $b = 0$. The asymmetric Gaussian (two Gaussians linked at the same point – the absolute maximum – with different standard deviations below and above this common point), used to analyze some MEIS experiments (Munoz-Marquez et al., 2005a; Okazawa et al., 2005) and the basic lineshape

$$\begin{aligned} f(\Delta E) &= \alpha \exp(-\alpha \Delta E)\Theta(\Delta E) * \text{gauss}(\Delta E, \sigma) \\ &= \frac{\alpha}{2} \exp\left(-\frac{\alpha}{2}(2\Delta E - \sigma^2 \alpha)\right)\left(1 + \text{erf}\left(\frac{\Delta E - \sigma^2 \alpha}{\sqrt{2}\sigma}\right)\right) \end{aligned} \tag{20}$$

proposed in Grande et al. (2006), are also displayed in Figure 9. All curves have the same standard deviation. For the basic lineshape, σ is the experimental resolution ($\sigma = \text{FWHM}/2.355$) and $\alpha = 1/\sigma_0$ (σ_0 from Figure 8) quantifies the effect of the single collision contribution.

Further advantages of the basic lineshape (Equation 20) are the following: (i) the corresponding self-convolutions are analytical and (ii) the Bothe–Landau equation (Sigmund, 2006) for an exponential decay energy-loss cross-section has also an analytical solution. Thus, the transport in a diluted medium can be easily computed. This is important for depth profiling techniques in amorphous targets.

5. Examples

The correct modeling of the energy-loss distribution in a single collision is very important for investigations of surface and near-surface interfaces as will be seen in the following examples.

5.1. Depth Profiling in Ultra Thin Films

Microelectronic devices based on metal-oxide-semiconductor (MOS) structures have continuously and exponentially advanced for decades without any substantial revolution regarding materials employed in integrated circuit fabrication. The main driving force for this tremendous evolution has been the downsizing of devices and integration.

Research of new gate oxide materials requires characterization tools in the nanometer scale, a straightforward consequence of the nanoscopic dimensions of the devices to which research is devoted. Medium energy ion scattering (MEIS) and narrow nuclear resonant reaction profiling (NRP) are the most important ion-beam characterization tools with nanometric depth resolution.

Gate oxides with high dielectric constant are currently being investigated to replace silicon oxide in MOS transistors. Hf-based oxides, silicates and aluminates are the best candidates for replacing SiO_2 as the gate dieletric because of their superior dielectric constant, electrical compatibility in the Si technology, and thermal and chemical stability (Wilk et al., 2001). Therefore, the depth profile of Hf in ultra thin films is of high importance.

In Figure 10 we show MEIS experimental results (the symbols) and the corresponding simulations for $Hf_{1.06}Zr_{0.1}O_2$ oxide with different thicknesses (see Figure 10 caption) taken with 100 keV protons (Pezzi et al., 2006). Here, the simulations (noted as standard ones) are based on Gaussian-shape energy-loss distributions, where the mean energy value has been taken from the SRIM code (Ziegler, 2006) and the straggling value from Chu's formula (Chu, 1976). We observe a decrease in the quality of the simulation for films with thicknesses smaller than one nanometer, when a homogenous oxide layer is assumed. Nevertheless, a good agreement can be obtained by fitting each spectrum, independently, without considering that they are in fact normalized to each other. Indeed, this is a pitfall,

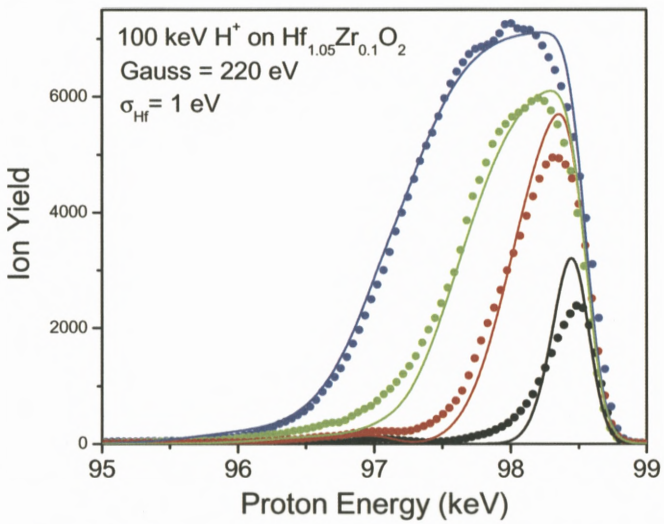

Figure 10. MEIS spectra obtained with 100 keV protons incident in thin HfO_2 (with small amount of Zr). The thicknesses of the films are 0.2 (black full circles), 0.5 (red full squares), 1 (green up triangles) and 2nm (blue down triangles).

since the corresponding thickness will not be realistic. Furthermore, as shown in Pezzi et al. (2006), the areal density of Hf as a function of the resulting film thickness as obtained by fitting the simulation results to the data in Figure 10 is a straight-line that has a large negative value of Hf when the thickness is extrapolated to zero.

On the other hand, when the energy-loss straggling during the strong head-on collision is included, agreement between experimental data and simulation is recovered, as shown in Figure 11.

Here we have used the basic lineshape from Equation 20 to describe the energy-loss distribution in a single, violent collision, responsible for the backscattering. The exponential decay α was obtained from Figure 8 for Hf, and amounts to 1/217 eV^{-1}. In this case the assumed experimental resolution of about 100 eV that is much smaller than used in Figure 10 because of the extra broadening arising from the backscattering collision. In addition, the total Hf quantity as a function of the film thickness is a linear function that crosses the origin (Pezzi et al., 2006).

5.2. Description of the Al Surface Peak

Medium-energy ion scattering (MEIS) in connection with shadowing and blocking techniques is a powerful method for the determination of structural and

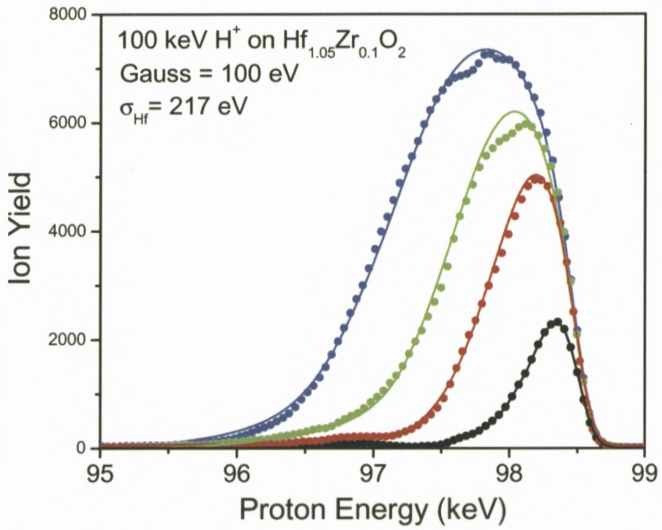

Figure 11. The same as in Figure 10 but the simulations include the effect a the energy loss spreading in a backscattering collisions.

vibrational parameters of crystalline surfaces (van der Veen, 1985). In this context, the shape of ion energy-loss spectra is usually not analyzed, because this requires a detailed knowledge on the energy-transfer mechanisms. Thus, standard energy-loss theories or semi-empirical methods based on Gaussian energy-loss distributions cannot be used successfully. Instead, an atomistic description of the electronic excitation process and its impact parameter dependence have to be taken into account in a stochastic approach which leads, in general, to an asymmetric line shape. Nevertheless, many groups use Gaussian line shapes to fit the surface peak area (using high resolution and grazing conditions) in order to get the fractions for adlayers or adatoms (Hoshino et al., 2005), which may lead to questionable interpretations by neglecting the asymmetry of all backscattered-ion distributions.

The surface peak is due to collisions at and near the surface, involving just the first few atomic layers. The deflection of incoming projectiles by surface atoms results in the formation of a volume behind this atom, practically free of ion trajectories, the so-called shadow cone. If the incident ion beam is aligned with a main axis of the crystal, shadowing greatly reduces the chance of backscattering from successive atoms along the row. In a similar way, the backscattered flux from sub-surface atoms cannot propagate in directions corresponding to vectors that point to atoms closer to the surface. This will result in pronounced minima

in the angular distribution of the backscattered flux. Such blocking dips provide a sensitive method to determine surface-atom displacements. An angular shift in the position of a blocking dip away from the bulk crystal blocking direction is a direct indication of layer relaxation. Accurate determination of structural parameters (atomic location and vibrational amplitudes) using Medium Energy Ion Scattering (MEIS) is a well-established technique. This is accomplished by comparing the angular scattering intensity to results of Monte-Carlo type computer simulations for models of the surface structure, as implemented, e.g., in the VEGAS (Frenken et al., 1986) code for trial atomic crystal structures. The atomic positions in the trial structure are changed until a convincing fit to the measured data (shape and minimum position) is obtained. This method, however, takes into account only the ballistic part of the backscattering events. The information contained in the detailed peak shape is usually not considered.

Since solid-state effects are of minor importance due to the large energy transfers involved, the valence-band contributions to the backscattering signal may therefore to a good approximation be described within an atomic model. This provides the best scenario for the use of advanced atomic-physics models, such as coupled-channel calculations.

Here we describe the energy-loss distribution of the surface peak for protons impinging with 60° (and $\phi = 35.3°$) with respect with the main axes of a clean Al(110) surface and being backscattered along a blocking direction also 60° off normal. Further details may be found in Grande et al. (2004) and Grande et al. (2005).

The configuration of the scattering experiment is schematically sketched in Figure 12(a). The top view of the Al(110) surface with a scattering plane perpendicular to the Al(110) surface is given in Figure 1(b). The incoming beam is aligned with the [−101] direction. For a bulk-terminated static lattice this geometry completely eliminates scattering events from all layers except the topmost one. Due to thermal vibrations and surface relaxation the deeper layers contribute to the surface peak as well.

5.2.1. *Transport: Stochastic and Monte-Carlo Approaches*

The energy lost by the projectile after several collisions is given by a series of convolutions of the energy-loss distribution for each single collision. Thus, each single collision is characterized by one impact parameter b_α. When a sequence of collisions is described by a set of impact parameters $\{b_\alpha\}$, for example along the incoming path before hitting the target nucleus, the energy-loss distribution of the projectile will be

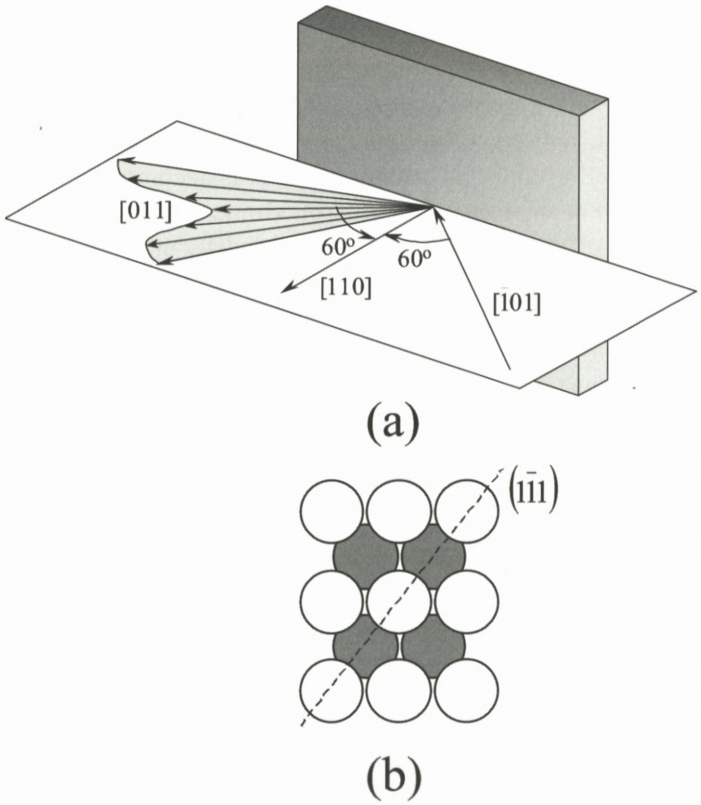

Figure 12. (a) Schematic figure of the scattering geometry used in this work; the scattering plane is shown in (b) in a top view of the Al(110) surface. Taken from Grande et al. (2004).

$$\frac{\mathrm{d}P_{\mathrm{in}}}{\mathrm{d}\Delta E}(\{b_\alpha\}) = \left(\prod_\alpha \int \mathrm{d}\Delta E_\alpha \frac{\mathrm{d}P_{\mathrm{atom}}}{\mathrm{d}\Delta E_\alpha}(b_\alpha)\right) \times \delta\left(\Delta E - \sum_\alpha \Delta E_\alpha\right). \tag{21}$$

The measurable sequences of impact parameters $\{b_\alpha\}$ are however only those that lead to a hitting event (a close backscattering encounter) and will depend on shadowing effects due to the atomic layers, which the ions pass through. In this way, the thermal vibrations as well as the relaxation of the first layers must also be

taken into account to determine the impact-parameter-averaged energy loss due to a target atom from the layer L' for the projectile that hits a target atom from layer L. The same holds true for the outgoing path after the backscattering. Then, the projectile energy distribution for a sequence of collisions that hit a target atom from layer L and reach the detector reads

$$
\begin{aligned}
Y_L(E) = & \prod_{L'=1}^{L} \int \mathrm{d}\Delta E_{L'}^{\mathrm{in}} \left(\frac{\mathrm{d}P_{\mathrm{atom}}}{\mathrm{d}\Delta E_{L'}^{\mathrm{in}}} \right)_{L',L}^{\mathrm{av}} \\
& \times \int \mathrm{d}\Delta E^{\mathrm{hit}} \left(\frac{\mathrm{d}P_{\mathrm{atom}}}{\mathrm{d}\Delta E^{\mathrm{hit}}}(b=0) \right) \\
& \times \prod_{L'=1}^{L} \int \mathrm{d}\Delta E_{L'}^{\mathrm{out}} \left(\frac{\mathrm{d}P_{\mathrm{atom}}}{\mathrm{d}\Delta E_{L'}^{\mathrm{out}}} \right)_{L',L}^{av} \\
& \times \delta \left\{ E - \left[K \left(E_0 - \sum_{L'} \Delta E_{L'}^{\mathrm{in}} - \frac{1}{2} \Delta E^{\mathrm{hit}} \right) - \sum_{L'} \Delta E_{L'}^{\mathrm{out}} - \frac{1}{2} \Delta E^{\mathrm{hit}} \right] \right\},
\end{aligned}
\tag{22}
$$

which turns out to be a series of convolutions. Here the symbol "av" stands for thermal averaging according to Grande et al. (2004), E_0 is the incident projectile energy and K is the kinematical factor describing the two-body kinematics for the backscattering collision. All impact parameters involved in the equations above are small compared to the L- and M-shell radii (they are given by the thermal vibrations of about 0.1 Å). We have assumed a straight-line motion for the incoming and outgoing ion path for the averaging of the energy-loss over the impact parameter. In fact the angular deviations affect the kinematical factor (Grande et al., 2004). All above energy distributions are by definition normalized to one. The measurable projectile energy-loss function can be determined by (neglecting the energy resolution of the detection system)

$$
Y_{\mathrm{detected}}(E) = \sum_{L} p_{\mathrm{HD}}(L) Y_L(E), \tag{23}
$$

where p_{HD} is the hitting-detecting probability for a backscattering collision at a given layer L. The hitting probability p_{H} is the chance to hit a certain target atom in a close backscattering encounter and will depend basically on shadowing effects due the layers the ions pass through. The detecting probability p_{D} is the chance for a particle emerging from that target position to leave the crystal in the detector direction and will depend strongly on blocking. For the upper layers p_{HD} is very close to the product of hitting p_{H} and detecting p_{D} probabilities as

observed also previously (Frenken et al., 1986). Thus, for the layers $L < 4$ the effect of connected in and out tracks is minor.

The surface peak was also calculated using the Monte-Carlo SILISH code (Munoz-Marquez et al., 2005c). As in the well-established VEGAS code, the lattice positions of the Y and Si atoms are stored in an array. For each impinging projectile the target atoms are displaced according to their one-dimensional root-mean-square thermal vibrations, and the ion trajectory is determined by a sequence of binary collisions. In each of them, the scattering angle is obtained by using the Moliere scattering potential, the ion energy and the impact parameter. The scattering angle is used to determine the new ion direction as well as the recoil-energy transfer to the target atom. This impact parameter is also used to select the associated inelastic energy-loss tabulated from calculations based on Equation (17) for different targets and impact parameters. The target atoms are selected by considering the atoms inside a cylinder with radius r_{max} and axis parallel to the ion incident direction. The flux of incident ions at each lattice position is then stored in a 2D matrix, where each bin, representing the transverse ion position, contains not only the number of projectiles, but also the histogram of ion directions and energy losses. The same calculation is performed for the outgoing ions in the detection direction using time reversibility. The incoming and outgoing tracks are connected by using the corresponding flux matrices, together with the position of the backscattering atom according to its thermal vibration. Only trajectories having the same scattering plane are connected. The corresponding energy loss for the whole ion trajectory therefore consists of the energy loss due to the incoming and outgoing paths, as well as to the elastic and inelastic energy loss in the hard scattering collision. In this way, the variation of the kinematical factor due to different scattering angles is also taken into account. While quite large values of the cylinder radius r_{max} (about 4 Å) are needed to fully converge the calculation, some improvement in computational speed was achieved without significant loss of precision by using a somewhat smaller value (about 2 Å) and including a correction to the final energy loss spectrum. Moreover, this method of calculation avoids "double counting" of energy losses from more distant atoms, which may fall into both the ingoing and outgoing trajectory cylinders if these cylinders are too large.

The energy-loss distribution of each visible backscattering layer is displayed in Figure 13. The contribution of the first layer corresponds to a single collision with the first atom on the Al surface (see Figure 3). The deeper layers involve differences in the impact-parameter distribution and a convolution of these layer-specific distributions. For backscattering layers $L > 3$ the resulting shape is approaching a Gaussian distribution, as expected for electronic energy-losses.

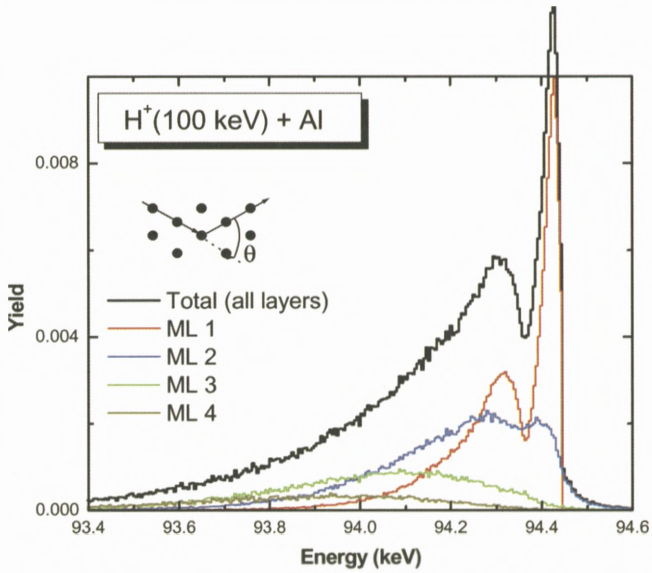

Figure 13. Contribution of each visible layer for the surface peak of 100 keV H^+ backscattered from the Al(110) surface for a 60–60 degree geometry.

According to Equation (23) the area of each curve in Figure 13 corresponds to the hitting-detecting probability p_{HD}. The backscattering yield of the first and second layers are similar because of a comparatively large surface relaxation, leading to a layer offset of about 0.1 Å. The third and fourth layers are still visible because of the thermal vibrations, which are of the order of the shadow cone radius for the ion energy used. For large energy losses even the fifth layer gains some importance. However, layers $L > 7$ have been neglected in the present work, since their contribution to the spectrum is very small.

The calculated curves in Figure 13 have been convoluted with the experimental resolution. The dashed curve AO (Atomic Orbital coupled-channel calculations) corresponds the simulations according to Equation (23) using a fixed impact parameter of $b = 0$ for the calculation of excitation/ionization probabilities in Al. The effect of the thermal vibrations along the ion history is represented by the dotted curve. Hence, the possible impact-parameters due to thermal vibrations are restricted to those outside of the shadow cone for a given hitting as well as detecting event. The solid curve includes additionally the effect of surface relaxation.

The results of the simulation show that although the surface relaxation is very important for the total yield, it affects the shape of energy-loss distribution very little. This is because backscattering collisions taking place in deep layers that

can contribute to the surface peak are due to trajectories having large impact parameters in the first layers (resulting in relatively insignificant energy losses) because of shadowing for the incoming path and blocking for the outgoing path. Thus, the surface relaxation plays a minor role for the energy-loss shape, but is very important for the total yield.

The simulation represented by the solid curve includes all-important terms that can be computed within the framework of the independent-electron model (IEM). In this simulation the effects concerning the electronic and atomic structure of Al(110) and ion-atom collisions including all higher-order effects have been very accurately included (within the IEM). Other effects such as a better description of the valence electrons, dynamically curved ion trajectories and/or the influence of a small H^0 charge-state fraction are of minor importance. This has been checked using test calculations. Furthermore, previous investigations have shown that correlated vibrations do only have a minor influence on the results (Frenken et al., 1986). Also the approximations used to calculate the impact-parameter distributions for each collision as well as the angular spreading have been cross-checked by performing full Monte-Carlo calculations SILISH. As can be observed in Figure 14, there is reasonable agreement between the present analytical simulation (solid line) and a full Monte-Carlo calculation for the same problem (dashed-dotted curve). The maximum relative deviation between both model results slightly exceeds 10% at backscattering energies below 93.8 keV.

The experimental data show a steeper decrease towards lower energies than our best analytical prediction (solid line) or the Monte-Carlo result (dashed-dotted curve). The remaining difference between both calculations and the experimental data clearly exceeds 30% at low backscattering energies, which is much larger than the present experimental and numerical uncertainties. We attribute this disagreement between the simulation and the experimental data to a breakdown of the independent-electron model (IEM). It was shown in Grande et al. (2005) that the dynamic modification of the target-electron density as well as the modification of the electron binding energy in multiple ionizations lead to a reduction of the ionization/excitation probabilities and are responsible for the observed differences. For other geometries these effects are expected to be of minor importance and a much better agreement with the experimental data have been observed (Grande et al., 2005).

6. Conclusions

Among other "unsolved" problems in IBA, the use of a more realistic (a non-Gaussian distribution) description for the electronic energy-loss distribution is

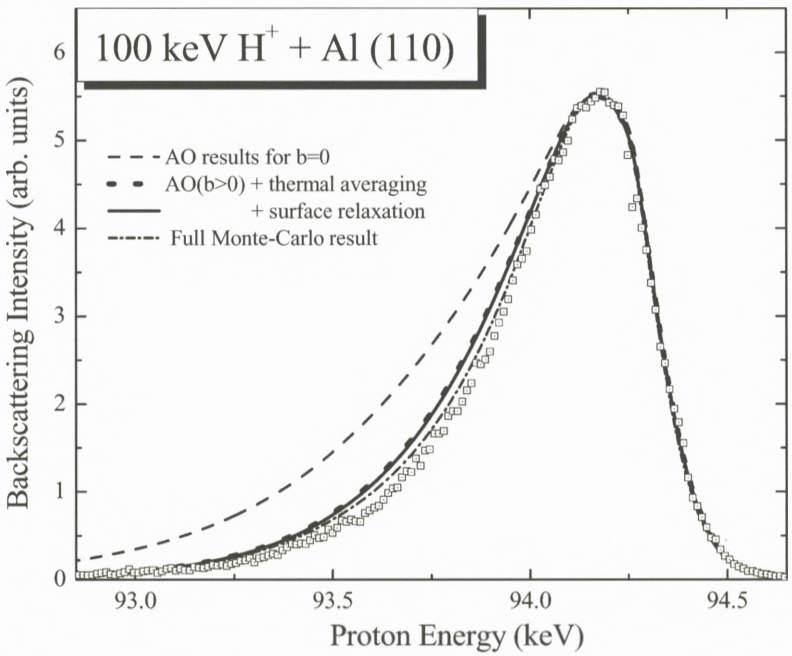

Figure 14. Experimental data (open squares) for 100 keV H^+ backscattered from Al(110) in comparison with simulations using the coupled-channel method (AO). Dashed line: energy-loss calculations for $b = 0$ only (no thermal averaging), weighted with the hitting-detecting probabilities. Dotted line: energy-loss calculations averaged over thermal vibrations and considering the weighted impact-parameter dependence of the energy-transfer distributions. Solid curve: energy-loss calculations including thermal vibrations and additionally the Al surface relaxation. Dashed-dotted curve: full Monte-Carlo calculations (SILISH) including thermal vibrations and surface relaxation.

crucial for high-resolution near-surface experiments. In this work we have shown some recent developments, which go far beyond the usual Gaussian approximation. In particular we have provided an accurate description of the energy-loss spectrum in a single collision using the coupled-channel method as well as the statistics of collisions (the ballistics) for amorphous and crystalline materials.

We have observed that large energy losses arising from inner-shell (e.g. the L-shell for Al) ionization/excitation are responsible for the energy-loss asymmetry at near central collisions (b close to zero) with a considerable fraction of double ionization. We note that the appropriate methods to handle the energy-loss in such violent collisions are those from the atomic physics field.

Using the coupled-channel calculations as a benchmark we have analyzed a simple energy-loss model for the energy-loss moments. Also, these *ab-initio*

calculations have been used to check some analytical formulas for the energy-loss distribution in order to replace the standard Gaussian distribution. Thus, the so-called basic lineshape is a step forward for near surface ion-beam analysis.

The energy loss in a single violent collision (as the backscattering collision in RBS or MEIS) firstly leads to a "degradation" of the depth resolution. Then, the real experimental resolution in high-resolution experiments is indeed often better than the one reported. For instance, concerning proton or He bombardment of few hundred keV, the difference between the nominal and real experimental resolution is large in the case of heavy targets (for RBS and MEIS) and less relevant for IBA techniques (such as NRA) involving light targets.

Nevertheless, as observed in the examples given in Section 5, the correct modeling of the energy-loss distribution is important to get reliable depth profiles in oxides and the shape of the surface peak.

Acknowledgements

This work was partially supported by CAPES -PROBRAL, by CNPq and by the Alexander-von-Humboldt foundation. Part of this work is a result of fruitful collaborations with D.P Woodruff (Warwick), T. Gustafsson (Rutgers), and M. Copel (IBM).

References

Arista N.R. (2002): Energy Loss of ions in solids: Non-linear calculations for slow and swift ions. Nucl Instr Methods **195**, 91–105

Arista N.R. and Lifschitz A. (1998): Velocity-dependent screening in metals. Phys Rev A **57**, 200–207

Bang J. and Hansteen J.M. (1959): IPM. Kgl Dan Vidensk Selsk Mat Fys Medd **31**, 13

Bloch F. (1933): The slow down of rapidly moving particles in the their passing through solid matter. Ann Physik **16**, 285

Carstanjen H.D. (1998): Ion beam analysis with monolayer resolution. Nucl Instr Methods **136–138**, 1183–1190

Chu W.K. (1976): Calculation of energy straggling for protons and He ions. Phys Rev A **13**, 2057–2060

Debus J., Schultz-Ertner D., Haberer T., Kraft G. and Jaekel O. (2004): Heavy charged particle therapy: From the technical challenge to the clinical role. Radiotherapy and Oncology **73**, 122

Dollinger G., Boulouednine M., Bergmaier A. and Faestermann T. (1998a): Nonequilibrium charge states of recoil ions in high resolution elastic recoil detection analysis. Nucl Instr Methods **136–138**, 574

Dollinger G., Frey C.M., Bergmaier A. and Faestermann T. (1998b): Elastic recoil detection with single atomic layer depth resolution. Nucl Instr Methods **136-138**, 603

Dollinger G., Bergmaier A., Goergens L., Neumaiera P., Vandervorst W. and Jakschik S. (2004): High resolution elastic recoil detection. Nucl Instr Methods **219–220**, 333

dos Santos J.H.R., Grande P.L., Behar M., Boudinov H. and Schiwietz G. (1997): Angular dependence of the electronic energy loss of 800-keV He ions along the Si[100] direction. Phys Rev B **55**, 4332–4342

Driemeier C., Miotti L., Pezzi R.P., Bastos K.P. and Baumvol I.J.R. (2006): The use of narrow nuclear resonances in the study of alternative metal-oxide semiconductor structures. Nucl Instr Methods Phys Res B **249**, 278–285

Frenken J.W.M., Tromp R.M. and van der Veen J.F. (1986): VEGAS code. Nucl Instr Methods **17**, 334

Grande P.L. and Schiwietz G. (1995): On classical calculations of the electronic stopping power at intermediate energies. J Phys B: At Mol Opt Phys **28**, 425–433

Grande P.L. and Schiwietz G. (1998): Impact-parameter dependence of the electronic energy loss of fast ions. Phys Rev A **58**, 3796–3801

Grande P.L. and Schiwietz G. (2002): The unitary convolution approximation for heavy ions. Nucl Instr Methods **195**, 55–63

Grande P.L. and Schiwietz G. (2004): Ionization and energy loss beyond perturbation theory – Advances in Quantum Chemistry, first edn., Elsevier Academic Press, Amsterdam

Grande P.L. and Schiwietz G. (2006): Convolution approximation for swift particles. Free download from `http://www.hmi.de/people/schiwietz/casp.html`

Grande P.L., Hentz A., Schiwietz G., Schulte W.H., Busch B.W., Starodub D. and Gustafsson T. (2004): Nonperturbative treatment of medium-energy proton scattering under shadowing-blocking conditions in Al(110). Phys Rev B **69**, 104112

Grande P.L., Hentz A., Schiwietz G., Starodub D., Garfunkel E. and Gustafsson T. (2005): Observation of collective inner-shell effects for protons backscattered from the Al(110) surface. Phys Rev A **72**, 012902

Grande P.L., Hentz A., Pezzi R.P. and Schiwietz G. (2006): Improved energy-loss formulas for high resolution ion-beam analysis. Nucl Instr Methods, to be published

Grüner F. and Bell F. (2006): First-principles-simulation of both charge state and stopping power of swift heavy ions in solids. Nucl Instr Methods **245**, 15–18

Herman F. and Skillmann S. (1963): *Atomic Structure Calculations*. Prentice-Hall, Inc. Englewood Cliffs, New Jersey, first edn.

Hoshino Y., Fukuyama R., Nishimura T., Tanaka S., Kohyama M. and Kido Y. (2005): Atomic structure of Si-rich 6H-Si(0001) – 2 × 2 surface. Phys Rev B **71**, 195331

McGuire N.S. and Simony P.R. (1981): Screening and anti-screening by projectile electrons in high-velocity atomic-collisions. Phys Rev A **24**, 97–102

Kabachnik N.M., Chumanova O.V. and Chumanov V.Y. (1993): Impact parameter dependence of energy-loss straggling in ion-atom collisions. Nucl Instr Methods **83**, 591–593

Kimura K., Ohshima K. and Mannami M. (1994): Monolayer analysis in Rutherford backscattering spectroscopy. Appl Phys Lett **64**, 2232–2234

Maurel B., Amsel G. and Nadai J.P. (1982): Depth profiling with narrow resonances of nuclear reactions: theory and experimental use. Nuclear Instr and Methods **197**, 1–13

McGuire J.H. and Weaver L. (1977): Independent electron approximation for atomic scattering by heavy particles. Phys Rev A **16**, 41–47

Mott N.F. (1931): On the theory of excitation by collision with heavy particles. Proc Cambr Phil Soc **27**, 553–560

Munoz-Marquez M.A., Parkinson G.S., Quinn P., Gladis M., Tanner R., Woodruff D.P., Bailey P. and Noakes T.C.Q. (2005a): N-induced pseudo-(100) reconstruction of Cu(111): One layer or more? Surf Sci **582**, 97–109

Munoz-Marquez M.A., Parkinson G.S., Woodruff D.P., Hentz A., Grande P.L., Schiwietz G., Wood T.J., Bonet C., Tear S.P., Bailey P. et al. (2005b): Energy loss in medium-energy ion scattering: A combined theoretical and experimental study of the model system Y on Si(111). Phys Rev B **72**, 075415 (pages 10). `http://link.aps.org/abstract/PRB/v72/e075415`

Munoz-Marquez M.A., Parkinson G.S., Woodruff D.P., Hentz A., Grande P.L., Schiwietz G., Wood T.J., Bonet C., Tear S.P., Bailey P. et al. (2005c): Energy loss in medium-energy ion scattering: A combined theoretical and experimental study of the model system Y on Si(111). Phys Rev B **72**, 075415

Okazawa T., Takeuchi F. and Kido Y. (2005): Enhanced and correlated thermal vibrations of Cu(111) and Ni(111) surfaces. Phys Rev B **72**, 075408

Olson R.E. (1989): Energy deposition by energetic heavy-ions in matter. Rad Eff and Deff in Solids **110**, 1–5

Pezzi R.P., Grande P.L., Copel M., Schiwietz G. and Baumvol I.J.R. (2006): Stochastic modeling of ion energy loss at intermediate energies: profiling with subnanometric resolution. Surf Sci, to be published

Rauhala E., Barradas N.P., Fazinic S., Mayer M., Szilagyi E. and Thompson M. (2006): Status of ion beam data analysis and simulation software. Nucl Instr Methods **244**, 436–456

Rösel F., Trautmann D. and Bauer G. (1982): Recoil effects in atomic inner shell ionization. Nucl Instr Methods **192**, 43–52

Ryufuku H. and Watanabe T. (1978): Charge transfer in collisions of atomic hydrogen with O^{8+}, He^{2+}, and H^{+}. Phys Rev A **18**, 2005–2015

Ryufuku H. and Watanabe T. (1979): Charge transfer cross sections for collisions of Li^{3+}, Be^{4+}, B^{5+}, and C^{6+} ions with atomic hydrogen. Phys Rev A **19**, 1538–1549

Schiwietz G. (1990): Coupled-channel calculation of stopping powers for intermediate-energy light-ions penetrating atomic H and He targets. Phys Rev A **42**, 296–306

Schiwietz G. and Grande P.L. (1999): A unitary convolution approximation for impact-parameter dependent electronic energy loss. Nucl Instr Methods **153**, 1–9

Schiwietz G., Wille U., Muiño R.D., Fainstein P.D. and Grande P.L. (1996): Comprehensive analysis of the stopping power of antiprotons and negative muons in He and H-2 gas targets. J Phys B: At Mol Opt Phys **29**, 307–321

Schiwietz G., Grande P.L. and Roth M. (2001): Electronic stopping of protons at intermediate velocities. ISL Annual Report HMI B587 (ISSN 1610-0638), 20

Schulte W.H., Busch B.W., Garfunkel E., Gustafsson T., Schiwietz G. and Grande P.L. (2001): Limitations to depth resolution in ion scattering experiments. Nucl Instr Methods **183**, 16–24

Sigmund P. (2004): Stopping of Heavy Ions – A Theoretical Approach, first edn., Springer, Berlin

Sigmund P. (2006): Particle Penetration and Radiation Effects, first edn. Springer, Berlin

Sigmund P. and Schinner A. (2000): Binary stopping theory for swift heavy ions. Europ Phys J D **12**, 425–434

Sigmund P. and Schinner A. (2002): Binary theory of the electronic stopping. Nucl Instr Methods **195**, 64–90

Srivastava S.K., Plachke D., Szokefalvi-Nagy A., Mayor J. and Carstanjen H.D. (2004): Counting individual atom layers in graphite – High-resolution RBS experiments on highly oriented pyrolytic graphite. Nucl Instr Methods **219–220**, 364–368

Tesmer J.R. and Nastasi M.A. (1995): Handbook of Modern Ion Beam Materials Analysis: Materials Research Society, first edn., MRS, Pittsburgh

van der Veen J.F. (1985): Ion beam crystallography of surfaces and interfaces. Surf Sci Rep **5**, 199–288

Vrijmoeth J., Zagwijn P.M., Frenken W.M. and van der Veen J.F. (1991): Monolayer resolution in Medium-Energy-Ion-Scaterring on $NiSi_2(111)$ surface. Phys Rev Lett **67**, 1134

Wilk G.D., Wallace R.M. and Anthony J.M. (2001): High-κ gate dielectrics: Current status and materials properties considerations. Appl Phys Rev **89**, 5243

Woodruff D.P. and Delchar T.A. (1994): Modern Techniques of Surface Science, second edn., Cambridge University Press, Cambridge

Ziegler J.F. (2006): SRIM code. Free download from `http://www.SRIM.org`